Sensors and Materials, Vol. 35, No. 9 (2023) 3211–3225
MYU Tokyo

S & M 3386

Development of 4-μm-pixel Pitch NIR Multispectral Imaging Sensor and Its Application to Glare-free NIR Color Fundus Camera

Motoshi Sobue,[1,2*] Hironari Takehara,[1] Makito Haruta,[1] Hiroyuki Tashiro,[1,3] Kiyotaka Sasagawa,[1] Ryo Kawasaki,[4] and Jun Ohta[1]

[1]Nara Institute of Science and Technology, Division of Materials Science, 8916-5 Takayama, Ikoma, Nara 630-0192, Japan
[2]Nanolux Co. Ltd., 8F Shinagawa Ground Central Tower, 2-16-4 Konan, Minato-ku, Tokyo 108-0075, Japan
[3]Kyushu University, Faculty of Medical Sciences, 3-1-1 Maidashi, Higashi-ku, Fukuoka 812-8582, Japan
[4]Osaka University, Division of Public Health, Department of Social Medicine, Graduate School of Medicine, 2-2 Yamadaoka, Suita, Osaka 565-0871, Japan

(Received February 18, 2023; accepted March 20, 2023)

Keywords: electrical biosensors, fundus camera, interference filter, IR color, multispectral imaging sensor

In this study, we describe the development of a compact NIR multispectral imaging sensor for use in glare-free NIR color fundus cameras. Integrating NIR technology into a fundus camera offers significant advantages over conventional RGB imaging using visible illumination, as it enables the glare-free capture of fundus images with minimal patient discomfort. The specifications necessary for a glare-free NIR color fundus camera were evaluated on the basis of factors such as pixel pitch size, pixel array layout, and multilayer interference filter design, in accordance with the camera's intended purpose. While multilayer interference filters were deposited on a glass substrate and bonded with the sensor chip in a 7.5 μm pixel pitch in a previous study, we propose an NIR multispectral imaging sensor directly depositing the interference filters on the wafer in a narrower 4 μm pixel pitch. In addition, the fabrication process for directly depositing NIR multispectral filters on the sensor wafer was proposed. The fabricated NIR multispectral imaging sensor was analyzed against the intended design. Finally, an NIR multispectral imaging sensor was installed on a glare-free NIR color fundus camera, and it was confirmed that the resulting camera is capable of providing medically relevant and meaningful information.

1. Introduction

Fundus images contain extensive health information, comprising tissues where the vascular system can be directly observed.[1–5] However, conventional visible light color fundus cameras use intense visible light flash illumination during imaging, which causes discomfort to patients. In addition, the images must be re-taken in case of an imaging failure. Moreover, pupil shrinkage

*Corresponding author: e-mail: sobue.motoshi.sk2@ms.naist.jp
https://doi.org/10.18494/SAM4358

ISSN 0914-4935

after the flashlight exposure increases the fundus imaging difficulty. In contrast, an NIR color fundus camera uses invisible NIR illumination, so patients do not feel glare. Thus, video recording can be performed, allowing the user to select the best images from the stored video images. The "glare-free" feature makes it easy to take video images and permits selfie fundus imaging, which is a significant advantage, especially in home healthcare. A glare-free NIR color fundus camera can detect vascular morphological changes associated with lifestyle-related diseases at an early stage.[6] The availability of non-invasive descriptions of vascular observations associated with high blood pressure, arteriosclerosis, obesity, and smoking, as well as non-invasive censoring methods to estimate blood concentrations of sugar and fat, enables the early detection of lifestyle-related diseases.[7] Early detection contributes to the risk stratification and visualization of lifestyle habit improvements and therapeutic effects. Thus, a glare-free NIR color fundus camera has excellent potential for use as a personal healthcare device and has broad applications for ophthalmologists and physicians, medical examinations, general practitioners, and patients using small inspection instruments in remote diagnoses. Making it compact and affordable is the key challenge as a "fundus camera anyone can use."[8–10] In a previous study,[11] it was identified that a single-chip IR multispectral image sensor, including an array of filters that transmit NIR light of different wavelengths to each pixel, is critical for providing a compact and affordable camera system. The previous study proposed an imaging sensor fabricated by bonding a glass substrate mosaic filter to an image sensor at a pixel pitch of 7.5 μm. However, a glass substrate bonding with a sensor chip is unsuitable for affordable and large-scale production. Moreover, the 7.5 μm pixel pitch is too large to be installed in a compact camera with the required resolution. In this study, we propose an NIR multispectral imaging sensor that directly deposits interference filters on a sensor wafer with a narrower pixel pitch of 4 μm. The proposed NIR multispectral sensor was installed in a glare-free NIR color fundus camera, and its fundus images were verified to deliver medically relevant and meaningful information. This research followed the Ethical Guidelines for Medical and Health Research Involving Human Subjects at the Nara Institute of Science and Technology.

2. Materials and Methods

2.1 Image sensor requirements and specifications

2.1.1 Base sensor selection

We selected a 1/2.6 inch sensor in consideration of compactness and affordability among the commercially available imaging sensors because an approximately 1/3 inch sensor is prevalent in a large surveillance market and is relatively low in price. The product name of the selected sensor is HM5533 manufactured by Himax Technologies, Inc. The selected sensor has a pixel pitch of 2 μm and a back-side-illuminated design. We considered two types of sensor candidates in the same format, namely, a standard sensor with a flat surface and an IR-enhanced sensor with an inverted pyramid array (IPA). We selected the standard type because the IR-enhanced type is more likely to cause cross-talk between pixels owing to an IPA surface in narrow pixel

pitches, resulting in inaccurate wavelength resolution.[12,13] This is particularly concerning because NIR light penetrates deep into silicon and generates photocarriers reaching the neighboring pixels,[14] whereas the selected sensor does not have mechanical solutions preventing cross-talk, for example, deep trenches between the pixels. Although a standard sensor may not exhibit the same level of IR sensitivity as an IR-enhanced sensor, particularly beyond 900 nm, we have prioritized wavelength resolution to attain the IR multispectral advantage. To counteract the low-sensitivity problems, as outlined in Sect. 2.1.3, we have employed a pixel array layout strategy. The specifications and relative quantum efficiency (QE) of the selected sensor are listed in Table 1 and Fig. 1, respectively.

2.1.2 Pixel binning optimization

We analyzed the optimal pixel pitch for this study because there is a trade-off between the spatial and wavelength resolutions based on the pixel pitch size. The spatial resolution is higher for smaller pixel pitches than for larger ones. However, the wavelength resolution is worse for smaller pixel pitches than that for larger ones, particularly in NIR, owing to greater interference between adjacent pixels. This interference is more significant in smaller pixels because the ratio

Table 1
Specifications of the selected sensor.

Item	Description
Sensitivity	1402 mV/Lux-sec
Sensor size	1/2.6 inch
Number of pixels	5.5 mega (2720 × 2080)
Pixel size	2.0 × 2.0 μm^2
Design	Back-side-illuminated design
Shutter	Rolling shutter
Maximum frame rate	30 FPS (2-lane MIPI), 45 FPS (4-lane MIPI)
Dynamic range	120 dB
S/N ratio (max)	37.33 dB
Video interface	MIPI-CSI2, 1 Gbps per lane
Output format	10-bit RAW
Power consumption (MIPI 4-lane 45 FPS)	171 mW (typ.)
Power consumption (MIPI 2-lane 30 FPS)	145 mW (typ.)

*Noted that the data was quoted from the manufacturer's datasheet.

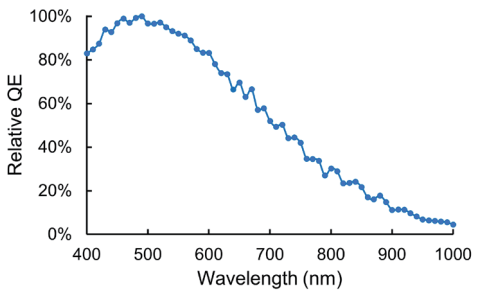

Fig. 1. (Color online) Relative QE of selected sensor without color filters.

of the length of the four sides to the overall area of a pixel is higher than that of larger pixels, resulting in a higher chance of cross-talk and a lower sensitivity of the targeted wavelength. In this study, given that the physical pixel size of the selected sensor is a pixel pitch of 2 μm, the alternatives for the pixel binning and effective pixel pitch include (a) single-pixel binning at 2 μm, (b) quad binning at 4 μm, and (c) 9-folded binning at a pixel pitch of 6 μm (Fig. 2).

To analyze optimal pixel binning, we first analyzed the spatial resolution requirements of this study. One of the critical requirements for the early detection of lifestyle-related diseases is the measurement of the relative thickness of the blood vessels. It is expected to have 10 pixels within 150-μm-diameter blood vessels in the fundus image to observe the shape of the blood vessels. Because the viewing angle of the fundus image is required to be at least 30 degrees around the center of the optic disk with 24 mm of the eye axial length of an average person, the target size of the image is calculated as 16.4 × 12.6 mm^2. The vertical resolution requirement is 838 pixels, which was calculated using the image size, target size, and resolution target, as shown in Fig. 3. The vertical resolutions of the 2, 4, and 6 μm pixels are 2080, 1040, and 693, respectively.

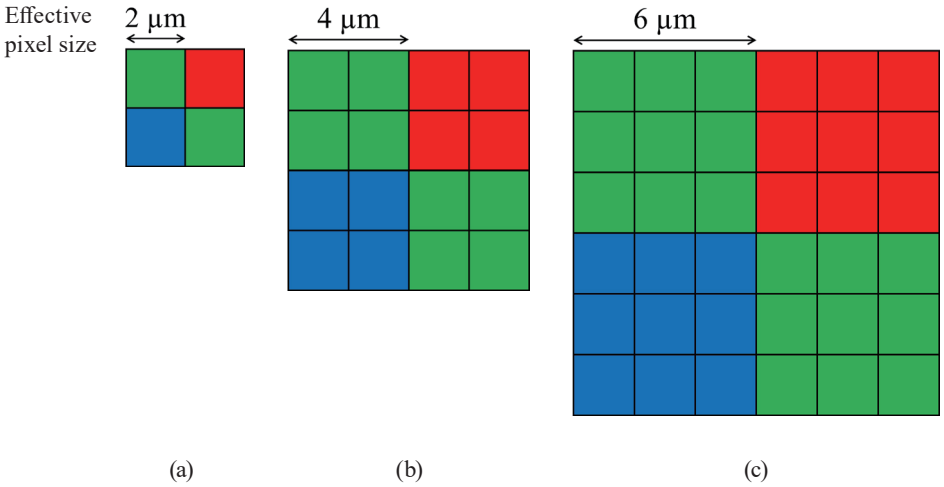

Fig. 2. (Color online) Pixel binning and effective pixel pitch: (a) single-pixel binning and effective pixel pitch of 2 μm, (b) quad binning and effective pixel pitch of 4 μm, and (c) 9-folded binning and effective pixel pitch of 6 μm.

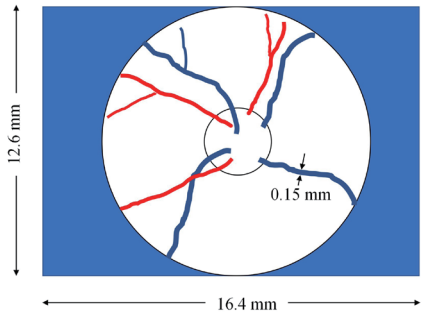

(a) Required angle: 30 degrees around optic disk
(b) Eye axial length: 24 mm (normal)
(c) Vertical image size: 12.6 mm, from (a) and (b)
(d) Horizontal image size: (c) × aspect ratio 1.3 = 16.4 mm
(e) Target size: 0.15 mm (150 μm)
(f) Resolution target: 10 pixels
(g) Vertical resolution requirement: (c)/(e) × (f) = 838 pixels
(h) Horizontal resolution requirement: (d)/(e) × (f) = 1096 pixels

Fig. 3. (Color online) Fundus camera resolution requirements.

Therefore, the spatial resolution of the pixel pitch of 6 μm (9-folded binning) does not meet the required standard, whereas the pixel pitches of 2 and 4 μm satisfy the requirements. Even considering the individual difference in eye axial length ranging from 23 to 26 mm, the analytical result is consistent as the vertical resolution requirement is in the range of 803–908 pixels, more than the vertical resolution of the pixel pitch of 6 μm (9-folded binning) but less than those of the pixel pitches of 2 and 4 μm.

Second, we assessed the wavelength resolutions of the 2, 4, and 6 μm pixel pitches. To analyze the pixel pitch and spectral performance, the optical flows in the multispectral filters were simulated using the three-dimensional finite-difference time-domain (FDTD) method, which can simulate various electric and magnetic materials using a personal computer. We built a multilayer interference filter structure, as discussed in Sect. 2.1.4, by arranging three different multilayer interference filters (800, 870, and 940 nm) set on the Bayer pattern in the simulation model. Specific wavelength light (800, 870, or 940 nm) illuminates the filter perpendicularly [Fig. 4(a)]. The horizontal grid size of the FDTD model was set as 51 × 51, 101 × 101, and 151 × 151 at pixel pitches of 2, 4, and 6 μm, respectively; the vertical grid size was set as 1529 for all pixel pitch sizes [Fig. 4(b)], balancing the robustness of the results and the computational time to convergence. In the simulation, light with a specific wavelength of 800, 870, or 940 nm was irradiated onto the pixels, and the transmittance of the target filter(s) was measured. The average transmittance rates of the two 800 nm filters with 800 nm light irradiation were 55.4, 63.8, and 70.6% at pixel pitches of 2, 4, and 6 μm, respectively [Fig. 4(c)]. The transmittance rates at 870 and 940 nm were above 90% for all pixel pitch sizes [Figs. 4(d) and 4(e)]. Our goal was to achieve a transmittance rate of 60% for all 800, 870, and 940 nm filters, based on the previous study where successful fundus images were obtained using IR1, IR2, and IR3 multilayer interference filters with an average transmittance rate of around 60%.[15] These simulation results showed that the pixel pitch of 2 μm (single pixel) at the 800 nm filter had a transmittance rate of 55.4% and did not meet the target (60%), whereas the 4 and 6 μm pixel pitches satisfied the requirements.

In summary, from the spatial and wavelength resolution performance characteristics, only the pixel pitch of 4 μm (quad binning) meets both the targets. The pixel pitch of 9 μm was too large to achieve the spatial resolution target and the pixel pitch of 2 μm was too small to achieve the wavelength resolution target (Table 2). Thus, we decided to deposit the multispectral filter on every four pixels through quad binning.

2.1.3 Pixel array layout

The pixel array layout is another important element in image sensor design. Most RGB sensors have a Bayer arrangement in which four pixels form one unit, with one pixel each for R and B, and two pixels for G.[16] In the previous study, the pixel array layout was IR1 (800 nm), IR2 (870 nm), and IR3 (940 nm) × 2 in a Bayer arrangement [Fig. 5(a)]. If the same filter arrangement is applied in this study, the sensitivity will be very low because of the low QE of the selected sensor in the NIR range, particularly above 900 nm. To resolve this issue, a modified filter arrangement was proposed by replacing two IR3 with two IR1 and shifting the wavelengths

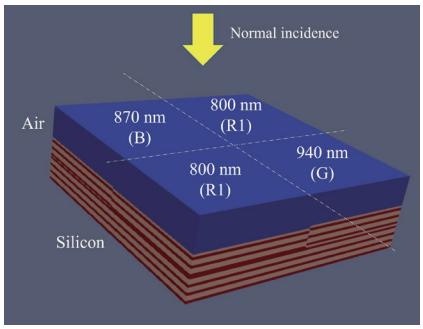

(a)

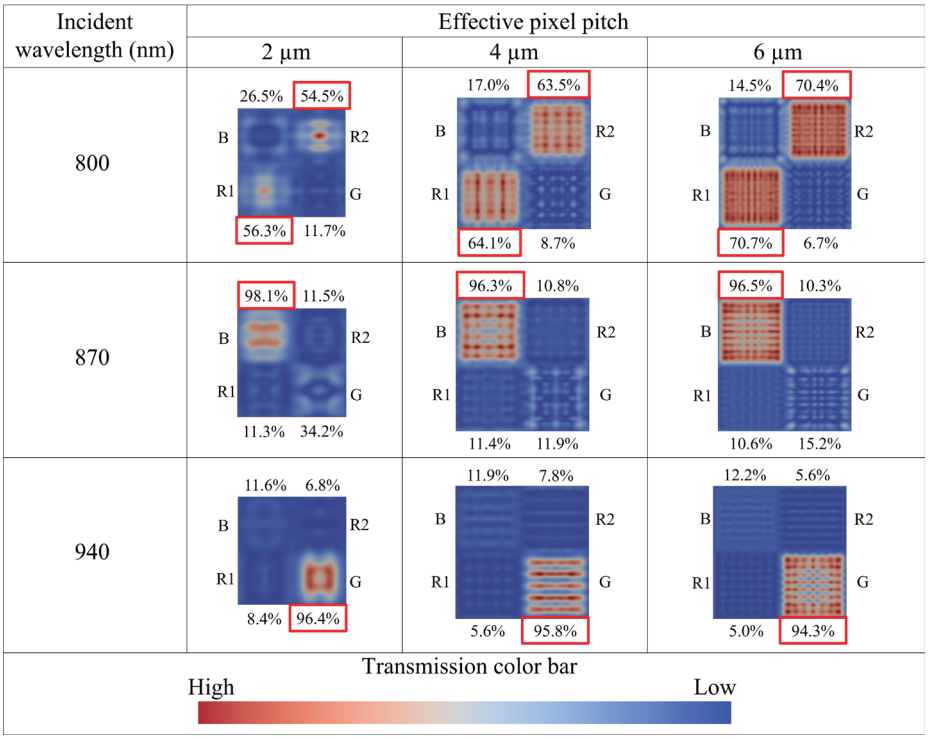

(b)

Fig. 4. (Color online) (a) Pixel array unit layout for three-dimensional simulation. The number on each pixel indicates the designed peak transmittance wavelength. (b) Calculated transmittance of each pixel for the effective pixel pitches of 2, 4, and 6 μm for incident light wavelengths of 800, 870, and 940 nm. The transmittances of pixels with the same wavelength of incident light and the designed peak transmittance wavelength are indicated by red rectangles.

Table 2
(Color online) Pixel pitches and evaluation results.

	Target	2 μm	4 μm	6 μm
Resolution: vertical pixels	873	2080	1040	693
Lowest % transmittance (%)	60	55.4	63.8	70.6

*Note that the hatched elements are above the target.

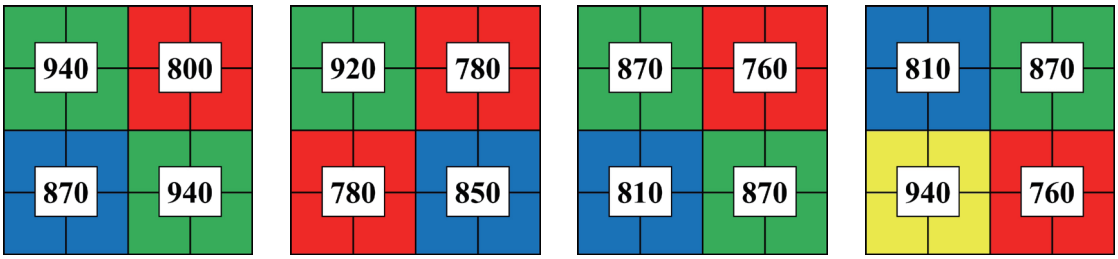

Fig. 5. (Color online) Filter array unit arrangements: (a) previous study, (b) this study – IR-color-oriented, (c) alternative 1 – sensitivity-oriented, and (d) alternative 2 – multispectral-oriented.

slightly shorter than that in the previous study to IR1 (780 nm), IR2 (850 nm), and IR3 (920 nm) [Fig. 5(b)]. The new filter arrangement was expected to enhance the total sensor sensitivity by reducing low-sensitivity wavelengths and increasing high-sensitivity wavelengths. The sensitivities of the selected sensor are 30, 16, and 8% at IR1 (800 nm), IR2 (870 nm), and IR3 (940 nm), respectively, as shown in Fig. 1; the average sensitivity per pixel is 16%. By modifying the pixel array as proposed, the average sensitivity per pixel will be improved to 25% or 1.6 times more than that in the previous study. Because the wavelength difference is only 20 nm, it is not considered to significantly impact the NIR color quality. We considered alternative pixel array layouts, as shown in Figs. 5(c) and 5(d). Figure 5(c) shows a layout aiming for enhanced sensitivity by shifting wavelengths much shorter than those in Fig. 5(b), and Fig. 5(d) shows a layout aiming for higher spectral resolution with four different multispectral filters. Although the layouts described in Figs. 5(c) and 5(d) are potentially advantageous, these do not fit this study because the wavelengths shorter than those in Fig. 5(b) are dazzling to human eyes and against the idea of a glare-free fundus camera. Therefore, we selected Fig. 5(b) as the pixel array layout for this study.

2.1.4 Multilayer interference filter design

The filter designs used to discriminate IR1 (780 nm), IR2 (850 nm), and IR3 (920 nm) were analyzed. Although visible RGB Bayer filters use absorption filters composed of pigments mixed with organic materials, no reliable absorption filter materials lie in the NIR range. In a previous study, a mosaic filter was fabricated using dielectric multilayer interference filters, which could be precisely designed using optical simulations, provided that the optical properties of the materials were known.[17] Fabry–Perot bandpass filters are significantly advantageous because a film with a half-wavelength thickness between the two mirrors can invert the reflected light phase, causing light close to the reference wavelength to be transmitted. Moreover, Fabry–Perot bandpass filters can control the transmission wavelength by adjusting the thickness of the intermediate layer. Because the thickness adjustment involves only one layer, the fabrication of a mosaic-like filter is relatively simple without numerous repetitive etching processes.

Multilayer designs of the interference filters are shown in Fig. 6(a). The bottom-half and top-half layers were common to all three filters. The only difference was the thickness of the intermediate layer. As indicated in Fig. 6(b), the transmission spectra of the filters can achieve the target wavelengths of IR1 (780 nm), IR2 (850 nm), and IR3 (920 nm) by the design. For the dielectric materials, we selected TiO_2 (a high-refractive-index material) and SiO_2 (a low-refractive-index material), which are commonly used non-metal materials in multilayer thin film factories. The total thickness of the filters is 1.5 μm, which is sufficiently small to apply to a pixel pitch of 4 μm.[15] While multilayer interference filters were deposited on a glass substrate and attached to a sensor chip in the previous study, in this study, the filters were deposited directly on the sensor wafer. This contributes to a significant cost reduction of the chip by eliminating the glass substrate and simplifying the fabrication process.

2.2 Fabrication process

We proposed a fabrication process for depositing multilayer interference filters onto a sensor wafer. Because the transmission wavelength can be controlled by simply adjusting the thickness of the intermediate layer, the fabrication of a mosaic-like filter is practically achievable. First, the bottom-half and intermediate stacks were deposited over the entire area. The deposition thickness of the intermediate layer was set on the basis of the thickness of the longest-wavelength bandpass filter [Fig. 7(a)]. The sites to be thinned were then patterned by lithography, followed by etching to achieve the required thickness of the intermediate layer. The same process was repeated to achieve three different thicknesses [Fig. 7(b)]. The deposition thicknesses were controlled by adjusting the deposition time, considering the pre-confirmed etching rate. The top-half of the layers were then deposited over the surface [Fig. 7(c)]. Finally, the filter materials in the pad areas were etched off for wire bonding [Fig. 7(d)].

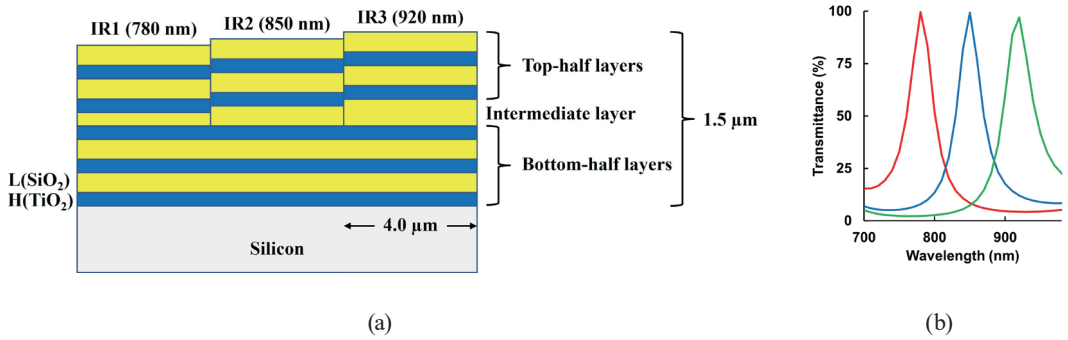

(a) (b)

Fig. 6. (Color online) (a) Multilayer interference filter designs and (b) simulated transmission spectra. Note that the layer number and the thicknesses are not accurately illustrated in Fig. 6(a).

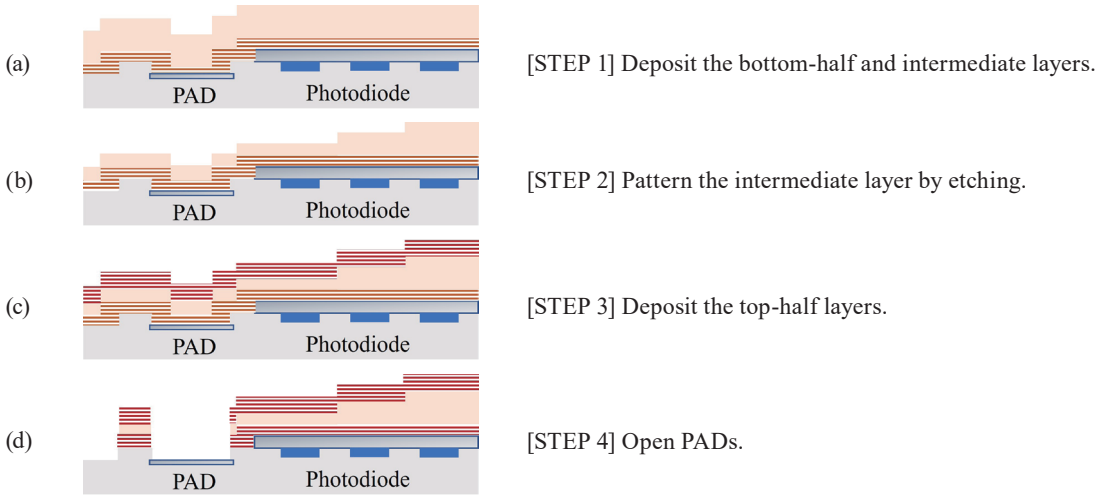

Fig. 7. (Color online) Filter fabrication process.

3. Results and Discussion

3.1 Spectral sensitivity and imaging results of the fabricated image sensor

The spectral responses of the IR1 (780 nm), IR2 (850 nm), and IR3 (920 nm) pixels of the fabricated sensor are shown in Fig. 8. With illumination perpendicular to the sensor surface, the spectral responses in the NIR region were measured every 10 nm using a monochromator. The spectral response [Fig. 8(b)] indicates that the three wavelengths of IR1 (780 nm), IR2 (850 nm), and IR3 (920 nm) were captured and isolated by the three different NIR multispectral filters. Two different IR1 (780 nm) filters indicated similar spectral responses despite the different adjacent filters. IR2 (850 nm) exhibited the highest peak, followed by IR1 (780 nm) and IR3 (920 nm).

The spectral responses are the products of the spectral sensitivity of the base sensor and filter transmittance. To evaluate the performance of the filters, the actual transmittance of the fabricated sensor was determined by dividing the spectral response by the base sensor sensitivity. These actual transmittances were then compared with the designed transmittance spectra of the multilayer interference filters, as shown in Fig. 9. The simulated peak transmittances of IR1, IR2, and IR3 were all almost 100%, and the average transmittances in the wavelength range of ±35 nm centered at each peak wavelength were 60, 60, and 65%, respectively. Here, the average values were calculated by dividing the integrated spectral transmittance over the wavelength by the integration range. Moreover, the ratios between the actual and designed peak transmittances of IR1 (780 nm), IR2 (850 nm), and IR3 (920 nm) were 61, 85, and 72%, respectively. The actual transmittance was the lowest in the IR1 (780 nm) filter, as analyzed by the 3D simulation [Figs. 4(c)–4(e)]. However, it was consistently observed that the actual transmittance of the fabricated filters was lower than the results obtained from 3D simulations; the actual transmittances were 61% compared with 64% obtained from the 3D simulation for IR1 (gap 3%), 85% compared with

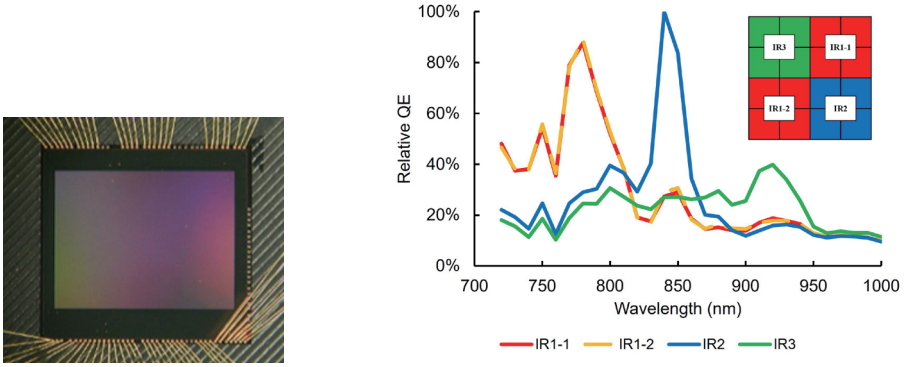

(a) (b)

Fig. 8. (Color online) (a) Fabricated sensor. (b) Spectral response of each multispectral filter in NIR region.

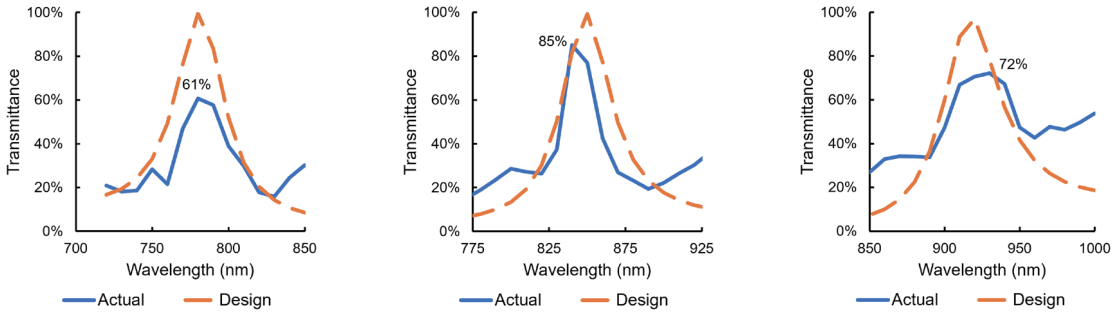

(a) (b) (c)

Fig. 9. (Color online) Actual and designed transmittances: (a) IR1 (780 nm), (b) IR2 (850 nm), and (c) IR3 (920 nm).

96% for IR2 (gap 11%), and 72% compared with 96% for IR3 (gap 24%). It is considered that the cross-talk in the fabricated sensor not only occurs in the multilayer filter layers but also in the silicon layer. In contrast, the 3D simulation accounts for cross-talk only in the multilayer filter layers. It was also observed that the gap between the actual results and the 3D simulations was larger at longer wavelengths. It is considered that a longer wavelength penetrates deeper into the silicon and crosses the pixels more. Cross-talk prevention is one of the key opportunities for improving the transmittance and spectral performance of multispectral imaging sensors in future research.

The fabricated NIR multispectral imaging sensor was installed in an NIR color camera. The NIR color technique is to generate RGB color estimates from NIR multispectral signals.[18–21] Figure 10 shows the outcome of processing the RAW images using the previously described methodology[11] for improving color quality. The pixel values obtained from the fabricated imaging sensor with the described spectral response were converted to values in ideal sensitivity characteristics modeled as normal distributions with a standard deviation of 15 nm centered at

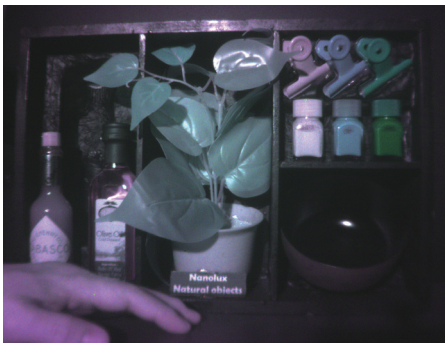

Fig. 10. (Color online) NIR color image obtained using the fabricated imaging sensor.

each peak wavelength. The conversion matrix $\boldsymbol{M}$ shown in Eq. (1) was used for the color space conversion. $\boldsymbol{M}$ was applied as in Eq. (2). Here, the pixel values of each channel (IR1, IR2, and IR3) acquired by the imaging sensor are indicated by the subscript 'raw', and the ones after conversion are indicated by the subscript 'conv'.

$$\boldsymbol{M} = \begin{bmatrix} 2.668 & -0.564 & -1.103 \\ -0.749 & 2.477 & -0.728 \\ -0.381 & -0.715 & 2.097 \end{bmatrix} \tag{1}$$

$$\begin{bmatrix} IR1_{conv} \\ IR2_{conv} \\ IR3_{conv} \end{bmatrix} = \boldsymbol{M} \begin{bmatrix} IR1_{raw} \\ IR2_{raw} \\ IR3_{raw} \end{bmatrix} \tag{2}$$

After the color space conversion process, the values of $IR1_{conv}$, $IR2_{conv}$, and $IR3_{conv}$ were subsequently reassigned to the R, B, and G values, respectively, in the sRGB color space, followed by brightness adjustment. Because the imaging sensor captures three different wavelengths, IR1 (780 nm), IR2 (850 nm), and IR3 (920 nm), an NIR color image was clearly delivered. The image is capable of differentiating the colors of objects as the colors of the ink bins, plant, and condiment bottles.

3.2 Fundus images and evaluation

The fabricated NIR multispectral imaging sensor was installed in a fundus camera system [Fig. 11(a)]. The sensor was mounted on a sensor board and connected to an image-processing board. While trans-palpebral, trans-scleral, and trans-pars-planar illumination methods from outside the pupil have been proposed for NIR illumination,[22–24] the optical system for this study was built using a Maxwellian illumination system such that collimated NIR light is reflected by a beam splitter and focused on the surface of the eye because it is widely used in conventional fundus cameras and less risky to accidental eye damage. Light is then spread to the

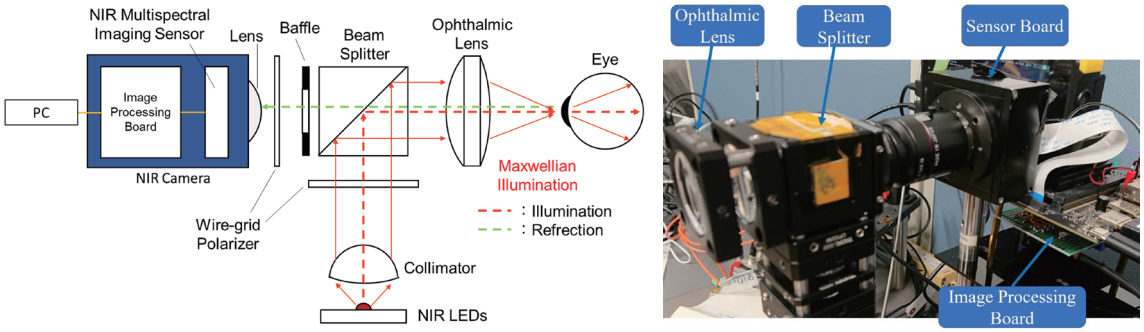

(a) (b)

Fig. 11. (Color online) Glare-free NIR color fundus camera with the fabricated sensor. (a) Camera components and (b) an appearance image.

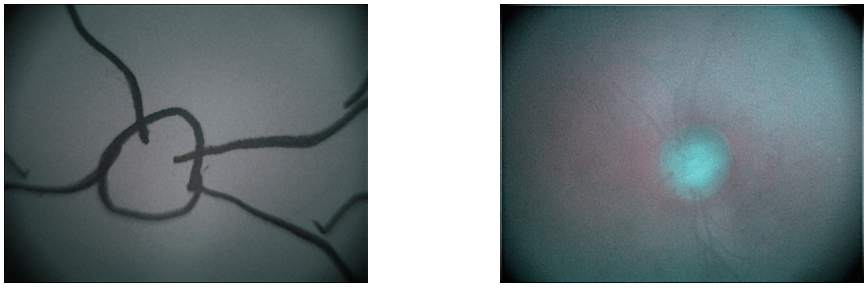

(a) (b)

Fig. 12. (Color online) Fundus images taken by glare-free NIR color fundus camera: (a) model and (b) human eyes.

retina by the ophthalmic lens. The light source used in the experiment was composed of LEDs assembled in a fiber line and emitted three wavelengths of IR1 (780 nm), IR2 (850 nm), and IR3 (920 nm).

To detect lifestyle-related diseases, fundus imaging was performed by focusing on the blood vessels around the optic disc. The shutter was opened when the illumination flashed spontaneously. The amount of illumination was controlled according to eye safety guidelines.

Figure 12 shows the acquired fundus images of model and human eyes. The optic disc and blood vessels were clearly visualized. The images were reviewed and confirmed by a medical doctor that the relative diameter and shape of blood vessels were sufficiently recognizable to observe the attenuation of retinal arterioles, focal arteriolar narrowing, the broadening of the arteriolar reflex, and minimal arteriolar-venous crossing defects. Consequently, hypertensive and atherosclerotic lifestyle-related diseases can be diagnosed on the basis of Scheie classification.[25] Thus, it is confirmed that an NIR glare-free fundus camera with a 4-μm-pixel pitch NIR multispectral imaging sensor can provide medically relevant and meaningful information.

4. Conclusions

A 4-μm-pixel pitch NIR multispectral imaging sensor was fabricated by directly depositing NIR multispectral filters on a sensor wafer. The sensor was applied to a glare-free NIR color fundus camera, and it was confirmed that the resulting camera was capable of providing medically relevant and meaningful information. As the goal of developing a "fundus camera anyone can use" is to make it compact and affordable, the successful outcomes of the fabricated sensor represent a significant step towards achieving this objective for healthcare purposes. One of the primary challenges that need to be addressed for the future improvement of NIR multispectral imaging sensors is the issue of cross-talk between pixels.

Acknowledgments

This study was supported by the Japan Science and Technology Agency, ACCEL (JPMJAC1601).

References

1 A. Kifley, J. J. Wang, S. Cugati, T. Y. Wong, and P. Mitchell: Microcirculation **15** (2008) 373. http://doi.wiley.com/10.1080/10739680701812220
2 R. Poplin, A. V. Varadarajan, K. Blumer, Y. Liu, M. V. McConnell, G. S. Corrado, L. Peng, and D. R. Webster: Nat. Biomed. Eng. **2** (2018) 158. https://www.nature.com/articles/s41551-018-0195-0
3 B. C. Bucca, D. M. Maahs, J. K. Snell-Bergeon, J. Hokanson, S. Rinella, F. Bishop, A. Boufard, J. Homann, C. Y. Cheung, and T. Y. Wong: J. Diabetes Complicat. **32** (2018) 234. https://linkinghub.elsevier.com/retrieve/pii/S1056872716308145
4 X. Hadoux, F. Hui, J. K. H. Lim, C. L. Masters, A. Pébay, S. Chevalier, J. Ha, S. Loi, C. J. Fowler, C. Rowe, V. L. Villemagne, E. N. Taylor, C. Fluke, J.-P. Soucy, F. Lesage, J.-P. Sylvestre, P. Rosa-Neto, S.Mathotaarachchi, S. Gauthier, Z. S. Nasreddine, J. D. Arbour, M.-A. Rhéaume, S. Beaulieu, M. Dirani, C. T. O. Nguyen, B. V. Bui, R. Williamson, J. G. Crowston, and P. van Wijngaarden: Nat. Commun. **10** (2019) 4227. https://doi.org/10.1038/s41467-019-12242-1
5 T. T. Nguyen, R. Kawasaki, J. J. Wang, A. J. Kreis, J. Shaw, W. Vilser, and T. Y. Wong: Diabetes Care **32** (2009) 2075. https://doi.org/10.2337/dc09-0075
6 M. Sobue, H. Takata, H. Takehara, M. Haruta, H. Tashiro, K. Sasagawa, R. Kawasaki, and J. Ohta: J. Robot. Mechatron. **34** (2022) 1152. https://www.fujipress.jp/jrm/rb/robot003400051152
7 Z. Wang, M. Uemura, H. Takehara, M. Haruta, H. Tashiro, K. Sasagawa, and J. Ohta: Jpn. J. Appl. Phys. **60** (2021) SBBL07. https://iopscience.iop.org/article/10.35848/1347-4065/abea4c
8 A. Pujari, G. Saluja, D. Agarwal, A. Sinha, A. P R, A. Kumar, and N. Sharma: Curr. Eye Res. **46** (2021) 1605. https://www.tandfonline.com/doi/full/10.1080/02713683.2021.1958347
9 C. H. Tan, B. M. Kyaw, H. Smith, C. S. Tan, and L. T. Car: J. Med. Internet Res. **22** (2020) e16658. http://www.jmir.org/2020/5/e16658/
10 M. W. M. Wintergerst, L. G. Jansen, F. G. Holz, and R. P. Finger: Asia-Pac. J. Ophthalmol. **9** (2020) 308. https://journals.lww.com/10.1097/APO.0000000000000303
11 H. Takehara, Z. Wang, H. Tang, N. Kishida, Y. Horiki, M. Sobue, M. Haruta, H. Tashiro, K. Sasagawa, and J. Ohta: ITE Trans. Media Technol. Appl. **10** (2022) 59. https://www.jstage.jst.go.jp/article/mta/10/2/10_59/_article
12 C. F. Han, J. M. Chiou, and J. F. Lin: Sensors **20** (2020) 3062. https://www.mdpi.com/1424-8220/20/11/3062
13 S. Yokogawa, I. Oshiyama, H. Ikeda, Y. Ebiko, T. Hirano, S. Saito, T. Oinoue, Y. Hagimoto, and H. Iwamoto: Sci. Rep. **7** (2017) 3832. https://www.nature.com/articles/s41598-017-04200-y
14 M. A. Green and M. J. Keevers: Prog. Photovoltaics Res. Appl. **3** (1995) 189. https://onlinelibrary.wiley.com/doi/10.1002/pip.4670030303
15 H. Takehara, H. Sumi, W. Ze, T. Kondo, M. Haruta, K. Sasagawa, and J. Ohta: Proc. 2019 IEEE Biomedical Circuits and Systems Conference (IEEE, 2019) 1–4.

16 Bayer. B: US Patent 3971065 (1976).
17 H. A. Macleod: Thin-Film Optical Filters (CRC Press, Taylor & Francis Group, FL, 2010) 4th ed., Chap. 2.
18 M. Sobue, H. Otake, H. Takehara, M. Haruta, H. Tashiro, K. Sasagawa, and J. Ohta: SPIE Int. Soc. Opt. Eng. **61** (2022) 063107. https://doi.org/10.1117/1.OE.61.6.063107
19 H. Sumi, H. Takehara, S. Miyazaki, D. Shirahige, K. Sasagawa, T. Tokuda, Y. Watanabe, N. Kishi, J. Ohta, and M. Ishikawa: Proc. 2018 IEEE Symposium on VLSI Technology (IEEE, 2018) 163–164.
20 Yasushi Nagamune: US Patent 8854472 (2014).
21 Yasushi Nagamune: US Patent 8836795 (2014).
22 D. Toslak, D. Thapa, Y. Chen, M. K. Erol, R. V. P. Chan, and X. Yao: Opt. Lett. **41** (2016) 2688. https://opg.optica.org/abstract.cfm?URI=ol-41-12-2688
23 B. Wang, D. Toslak, M. N. Alam, R. V. P. Chan, and X. Yao: Sci. Rep. **8** (2018) 8768. https://www.nature.com/articles/s41598-018-27112-x
24 C. L. Shields: Arch. Ophthalmol. **121** (2003) 1603. http://archopht.jamanetwork.com/article.aspx?doi=10.1001/archopht.121.11.1603
25 R. E. Rakel and D. Rakel: Textbook of Family Medicine (Elsevier, PA, 2011) 8th ed., Chap. 41.

About the Authors

Motoshi Sobue received his MS degree in engineering from Waseda University, Japan, in 1989 and his MA degree in economics from Duke University, USA, in 1996. He worked for the Bank of Japan, Intel, Dell, and BAT. In 2021, he joined the Graduate School of Material Science, Nara Institute of Science and Technology (NAIST), Nara, Japan, as a Ph.D. candidate. He is currently the CEO of Nanolux Co. Ltd.

Hironari Takehara received his ME degree in applied chemistry from Kansai University, Osaka, Japan, in 1986, and his Ph.D. degree in materials science from Nara Institute of Science and Technology (NAIST), Nara, Japan, in 2015. From 1986 to 2012, he was a semiconductor process engineer at Panasonic Corporation, Kyoto, Japan. In 2015 and 2019, he joined NAIST as a postdoctoral fellow and an assistant professor, respectively. His current research interests involve CMOS image sensors and bioimaging.

Makito Haruta received his MS degree in biological science and Dr. Eng. degree in material science from Nara Institute of Science and Technology (NAIST), Nara, Japan, in 2011 and 2014, respectively. He joined NAIST in 2016 as an assistant professor. In 2019, he joined the Graduate School of Science and Technology of NAIST as an assistant professor. His research interests include brain imaging devices for understanding brain functions related to animal behaviors.

Hiroyuki Tashiro received his ME degree from Toyohashi University of Technology in 1996 and his Ph.D. degree from Nara Institute of Science and Technology (NAIST) in 2017. In 1998, he joined Nidek Co., Ltd., working on the R&D of ophthalmic surgical systems and retinal prostheses. He has been an assistant professor in Kyushu University since 2014 and an associate professor at NAIST since 2019. His current research interests include artificial vision systems and neural interface.

Kiyotaka Sasagawa received his BS degree from Kyoto University in 1999 and his ME and Ph.D. degrees in materials science from NAIST, Japan, in 2001 and 2004, respectively. Then, he worked as a researcher at the National Institute of Information and Communications Technology, Tokyo. In 2008, he joined NAIST as an assistant professor and was promoted to an associate professor in 2019. His research interests include bioimaging, biosensing, and electromagnetic field imaging.

Ryo Kawasaki received his MD (1997) and Ph.D. (2008) degrees from Yamagata University, Japan, and MPH degree (2007) from Johns Hopkins University Bloomberg School of Public Health, USA. He is a physician-scientist in ophthalmology. His current research interests include retinal image analysis using artificial intelligence, epidemiology, preventive medicine, and community health.

Jun Ohta received his ME and Dr. Eng degrees in applied physics from The University of Tokyo, Japan, in 1983 and 1992, respectively. In 1983, he joined Mitsubishi Electric Corporation, Japan. In 1998, he joined Nara Institute of Science and Technology (NAIST), Japan, and was appointed as a professor in 2004. His research interests include smart CMOS image sensors for biomedical applications. He is a Fellow of IEEE, the Japan Society of Applied Physics, and ITE.